From Photography to Microbiology: Eigenbiome Models for Skin Appearance

Parneet Kaur
Rutgers University
parneet@rutgers.edu

Kristin J. Dana
Rutgers University
kdana@ece.rutgers.edu

Gabriela Oana Cula
Johnson & Johnson
GCula@its.jnj.com

Abstract

Skin appearance modeling using high resolution photography has led to advances in recognition, rendering and analysis. Computational appearance provides an exciting new opportunity for integrating macroscopic imaging and microscopic biology. Recent studies indicate that skin appearance is dependent on the unseen distribution of microbes on the skin surface, i.e. the skin microbiome. While modern sequencing methods can be used to identify microbes, these methods are costly and time-consuming. We develop a computational skin texture model to characterize image-based patterns and link them to underlying microbiome clusters. The pattern analysis uses ultraviolet and blue fluorescence multimodal skin photography. The intersection of appearance and microbiome clusters reveals a pattern of microbiome that is predictable with high accuracy based on skin appearance. Furthermore, the use of non-negative matrix factorization allows a representation of the microbiome eigenvector as a physically plausible positive distribution of bacterial components. In this paper, we present the first results in this area of predicting microbiome clusters based on computational skin texture.

1. Introduction

Recent advances in measuring and analyzing the skin microbiome through gene sequencing is revolutionizing our understanding of skin appearance. With skin microbiome measurements, causative relationships between microbes and macro-appearance can be explored. However, gene sequencing is very cost-prohibitive and time-consuming. An exciting opportunity exists to use *photographic imaging and appearance modeling to infer the skin microbiome*, i.e. to effectively "see" the microbiome of a human subject by analyzing skin surface patterns. The pioneering work of [14] shows that healthy skin may harbor a particular strain of benevolent bacteria. The appearance of human skin in this study was divided manually into only two simple classes of good and bad skin appearance. By developing computa-
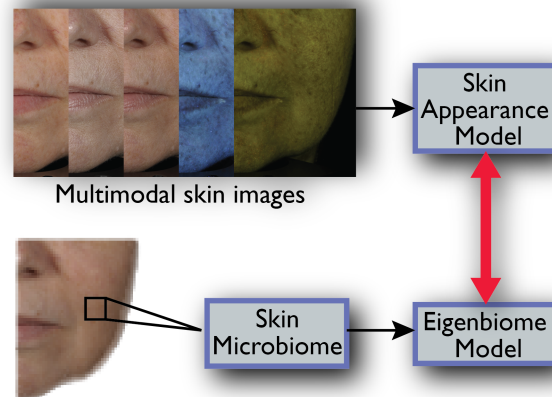

Figure 1: The computational skin appearance model characterizes multimodal images based on their attributes using a texton-based approach. The eigenbiome model projects the skin microbiome to a lower dimensional subspace. By identifying overlapping groups in appearance and microbiome clusters, we show that our skin appearance model is predictive of the underlying microbiome clusters.

tional models of skin appearance, we provide a more fine-grained quantitative categorization of human subjects using multiple classes of appearance. While prior work in microbiomics shows the association of bacteria with skin appearance [14, 24, 19], there is no mechanism for automatic inference of the skin microbiome from images. This association of visual patterns to bio-patterns on the skin surface is a novel area that has not been explored.

In this paper, we present an approach that uses multimodal skin imaging and sparse coding to link microbiome to skin texture (Figure 1). For computational skin texture, we use a texton-based approach with a neural network classifier to categorize skin regions based on the distribution of known attributes. The eigenbiome model projects the skin microbiome to a lower dimensional subspace. Projections of microbiome using non-negative matrix factorization (NMF) reveal a physically realizable eigenbiome where
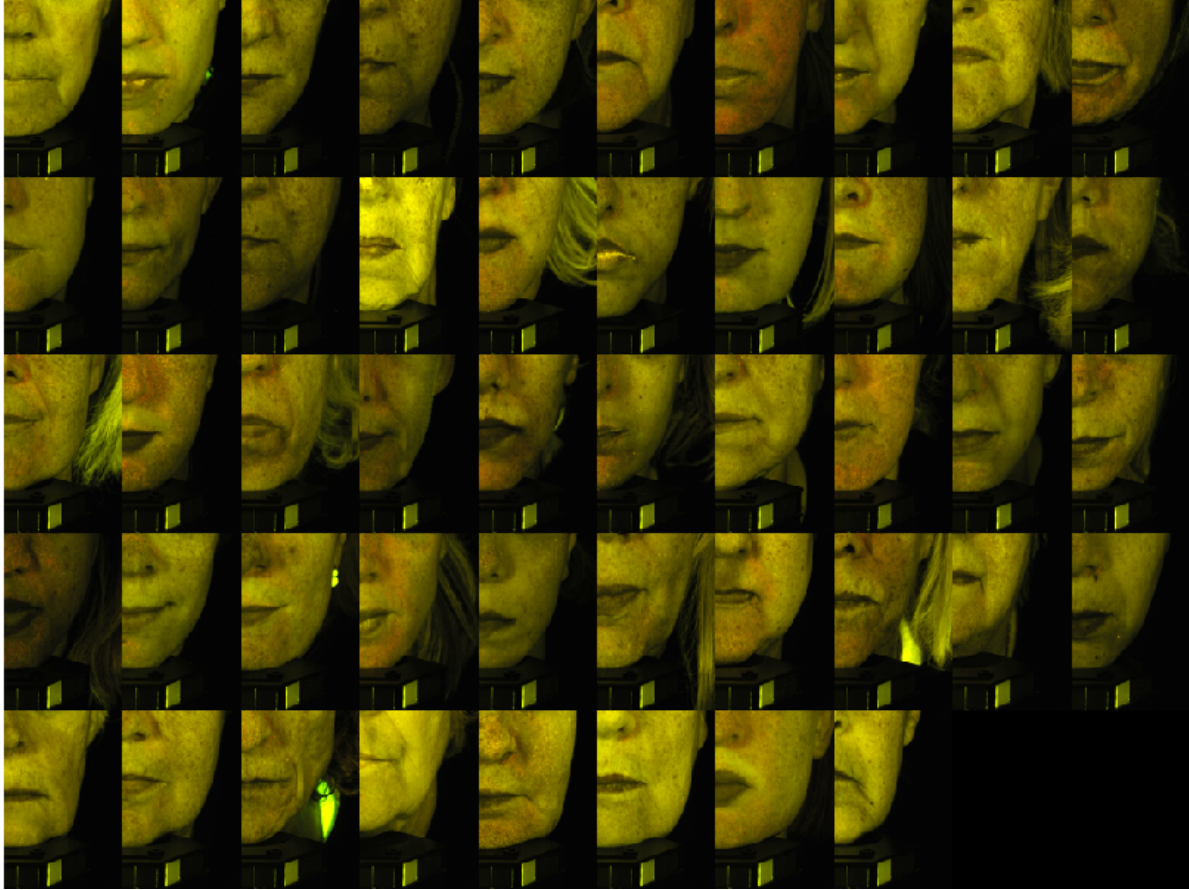
Figure 2: Partial faces of subjects imaged in fluorescence excitation with blue-light (FLUO) modality. Our database contains 48 subjects with age varying between 25 and 68. The faces of each subject are imaged from left, right and frontal views under five modalities. Each image is 4032×6048 pixels in size. The forehead regions used in our experiments are from the frontal views.

the eigenvectors are all positive components and represent particular concentrations of microbes. For our experiments, we capture appearance measurements from 48 human subjects with multimodal images: fluorescence excitation with blue-light (FLUO), fluorescence excitation with ultraviolet radiation (UV), parallel polarization (PPOL), cross polarization (XPOL) and visible light (VISI) (Figures 2 and 3). The association of appearance and microbiome is observed with FLUO and UV imaging modalities, therefore these modalities are used for our experiments. Sequencing of swabs from the forehead skin of the 48 subjects gives the corresponding skin microbiome. Using both eigenbiome and skin texton modeling, we have identified overlapping groups in appearance and microbiome. We show that our skin appearance models are predictive of the underlying microbiome clusters. Therefore, convenient and instantaneous multi-modal photography may be sufficient for inferring microbial characteristics. This proposed methodology

is the first of its kind to use a computational model of skin macro-appearance to predict the microbiome clusters.

2. Related Work

Human skin is a complex, multi-layered structure, which hosts various microbial communities. Studies of the skin microbiome [2, 40, 18] show dependence on genetics, environment and lifestyle as well as a variation over time. The skin microbiome varies according to the location on the body and from individual to individual. While the benefits of gut microbes are well known, knowledge of the skin microbiome is at an early stage [14, 24, 19].

Prior applications of skin modeling include studies of skin aging [4, 27, 38], computer-assisted quantitative dermatology [32, 44], and lesion classification [25, 34]. Several imaging techniques have been developed in dermatology for analyzing skin health. These imaging techniques include polarized imaging to enhance surface and subsurface
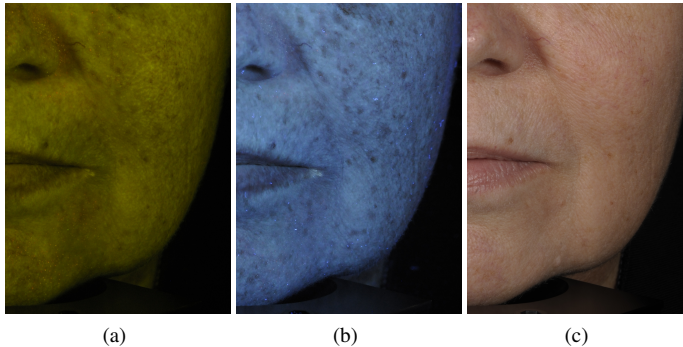
Figure 3: Facial images of a subject captured in different modalities. (a) Fluorescence excitation with blue-light (appears green). (b) Fluorescence excitation with UV radiation (appears blue). (c) Visible light. Fluorescence excitation captures skin textures not revealed by the visible light. The most salient attributes are apparent in FLUO and UV images (see Figure 4), therefore these modalities are used for computational skin modeling.

skin features, and fluorescence imaging to capture features which are not visible [23, 3, 21, 8, 9, 33]. The images captured using different methods are collectively called *multimodal images*. Multimodal high-resolution skin imaging captures fine scale features like pores, wrinkles, pigmentation. Computational methods have been developed to automatically detect skin conditions like inflammatory acne, erythema and facial sebum distribution from multimodal images [3, 21, 20]. However, the skin appearance has not been characterized as a collection of quantifiable features using these imaging techniques.

In computer vision, textons have been used for texture classification and object recognition. A classic approach is to use filter responses or the joint distribution of intensity values over pixel neighborhoods to identify the basic texture elements or textons [29, 5, 45, 10, 7, 31]. An image can then be represented by a distribution of textons. In [30], a multi-layered approach based on multilevel PCA and multiscale texon features is applied for face recognition. The bag-of-words representation of images using local interest features has been used for object or scene recognition [48, 13], image segmentation [22] and image retrieval [51]. Skin exhibits 3D texture and the appearance varies significantly depending on illumination or viewing direction. Methods have been developed to model skin appearance to account for this variation [6, 8, 29, 36]. Skin reflectance models have also been developed to acquire and render human skin [12, 15, 26, 47]. Local appearance has been linked to attributes [41, 1, 43], pose [42, 50, 35] and motion [39, 49, 46]. In this work we develop an appearance model that can be demonstrably linked to microbiome measurements.

3. Methods

3.1. Multimodal Skin Imaging

Fluorescence excitation with blue light (FLUO) or ultraviolet-A radiation (UV) is used to excite skin elements like keratin, collagen cross-links and elastin cross-links [23, 20]. These skin structures result in image features but not in visible light. Noticeable skin features include red or yellow dots in FLUO images (Figures 4(e) and 4(f)) and blotches in UV images (Figure 4(h)). Red dots in FLUO images are due to excitation of porphyrins in the pores. Porphyrins are known to be produced by bacteria such as Propionibacterium acnes residing in sebaceous glands. Yellow dots in FLUO images are produced by excitation of "horn" in pores, which is a mixture of keratinocyte ghosts from the sebaceous glands lining, sebaceous lipids, sebocyte ghosts and water. In UV images, blotches are observed due to skin pigmentation, which can be a result of pigmented macules (spots), hyperpigmentation due to sun-damage or conditions such as melasma, or erythematous macules (flat red lesions). Pigmented skin appears as dark patches in UV images as a result of attenuation by melanin in epidermis or induction of collagen cross-links fluorescence in dermis.

We capture images of 48 subjects with age varying between 25 and 68. The face of each subject is imaged from left, right and frontal views under five modalities: ultraviolet (UV), blue fluorescence (FLUO), parallel polarization (PPOL), cross polarization (XPOL) and visible light (VISI). Each image is 4032×6048 pixels in size. The most salient attributes are apparent in FLUO and UV images (Figure 4), therefore these modalities are used for computational skin modeling. The forehead regions used in our experiments are from the frontal views. Example images of these modalities are shown in Figure 3.
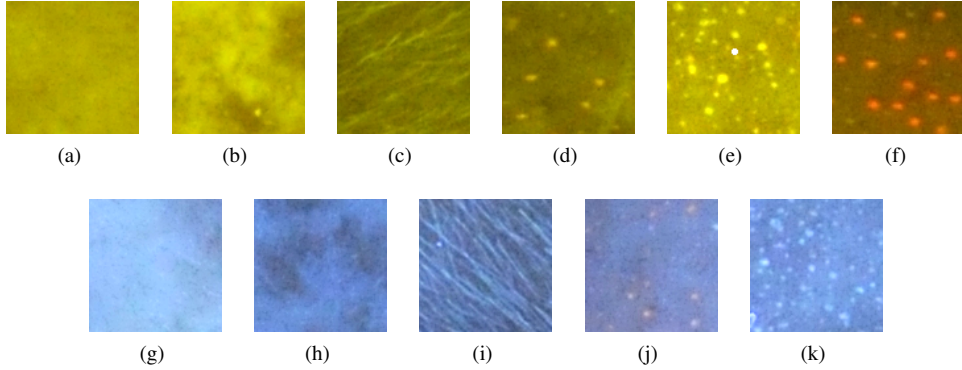
Figure 4: Examples of patches on facial skin. The corresponding attribute labels are as follows: In FLUO images: (a) smooth, (b) blotchy, (c) fine hair, (d) sparse sebum dots, (e) dense yellow sebum dots, (f) dense red sebum dots. In UV images: (g) smooth, (h) blotchy, (i) fine hair, (j) sparse sebum dots, (k) dense sebum dots.
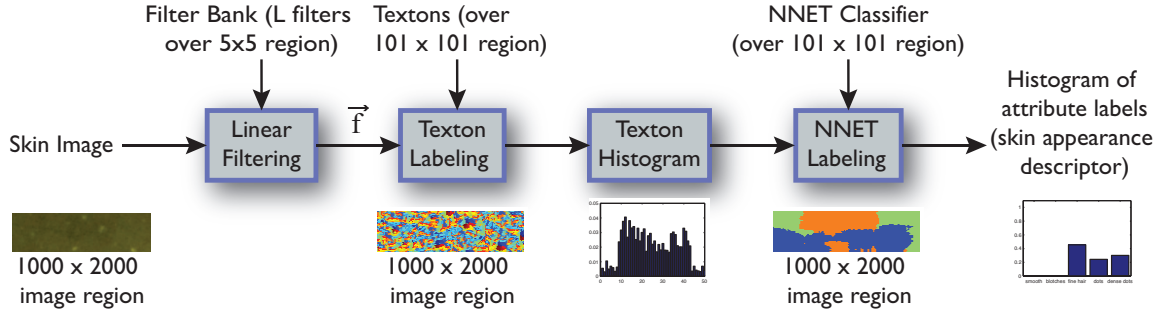

Figure 5: Computational appearance model. The texton histogram of a patch centered at each pixel of a skin image is labeled with one of the attribute categories using a neural networks classifier. The histogram of attribute labels of the entire skin image is its skin appearance descriptor. A texton label characterizes a 5×5 region. An attribute label characterizes a 101×101 region. The histogram of attribute labels describes a larger region (typical size 1000×2000)

3.2. Computational Appearance Modeling

In each modality, there are groups of people with perceptually similar skin appearance attributes. In FLUO and UV modalities, we observe the following five skin attributes: *smooth, blotchy, fine hair and sparse sebum dots or dense sebum dots* (Figure 4). We further categorize the *sebum dots* into red or yellow for the FLUO modality. The skin appearance of subjects can be modeled as a percentage of each of these attributes. This attribute-based approach includes a training phase to obtain a trained neural network (NNET) classifier [37] and an image labeling phase to obtain a skin appearance descriptor.

For the training phase, we use two components that are typical in computer vision: texton histograms which is an unsupervised approach, followed by a NNET classifier which is a supervised learning approach. To obtain a texton library, a random sampling of skin images are filtered using a filter bank with L filters, resulting in each pixel having an L-dimensional feature vector. Our filter bank is comprised of 48 filters as in [29]. These filters include 36 first and second order derivative of Gaussain filters (6 orientations, 3 scales each), 8 Laplacian of Gaussain filters and 4 Gaussian filters. The filter outputs over 5×5 region are clustered using k-means clustering into T clusters or textons. We empirically choose T=50 for our texton library.

A neural network classifier for each modality is trained to classify the skin patches. Every patch pixel is assigned the label of its closest texton and a texton histogram is computed over each skin patch of size 101×101. The training set is obtained by manually labeling random skin patches with one of the attribute labels described in Figure 4. The texton histograms from the labeled skin patches and the patch attribute labels are used for training the neural networks classifier (NNET).

The image labeling phase is illustrated in Figure 5. The term *skin image* refers to the entire extracted forehead region and a histogram of attributes (one attribute per patch) is used to to describe the skin image. For a skin image (typ-
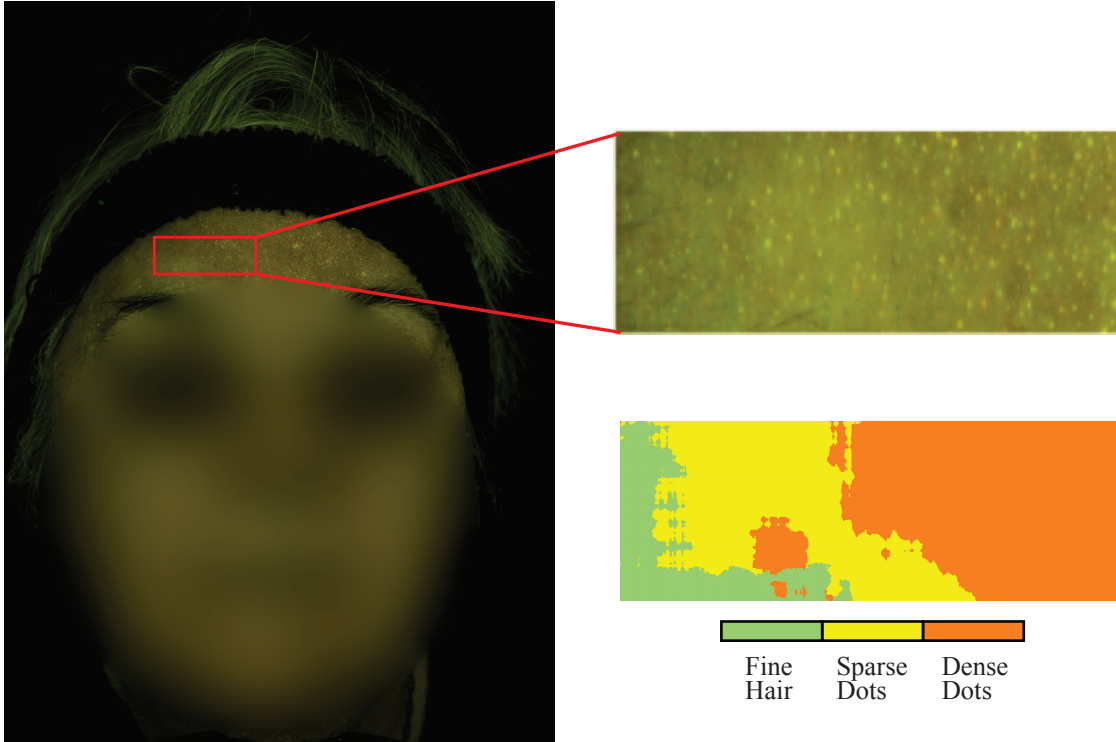
Figure 6: Image labeling using NNET classifier. The forehead skin image from the frontal view of the subject in FLUO modality has been labeled using NNET classifier. Face is blurred to preserve the privacy of the subject.

ical size 1000×2000), a patch of size 101×101 around each pixel is filtered, labeled with textons and a texton histogram is obtained. Using the texton histogram as input to the trained NNET classifer, the patch corresponding to each pixel is labeled with one of the attributes (for example Figure 6). A histogram of attribute labels is then constructed for each skin image, giving a skin appearance descriptor. We merge the attributes labels *sparse sebum dots* and *dense sebum dots* together to form the attribute *sebum dots*. In FLUO modality the color of the dots is an additional attribute that indicates either excitation of porphyrins (red sebum dots) or horn (yellow sebum dots). The dots are detected by finding high gradient pixels that have attribute labels as *sebum dots*. The mean of the normalized red channel for the dot pixels is a measure of dot redness.

Skin appearance of a subject is grouped using the percentage of attributes in each modality. Appearance clusters corresponding to each attribute are defined by specifying a simple threshold on the attribute percentages. For example, when the percentage of pixels in UV labeled as *sebum dots* is high ($\geq 50\%$), that subject is in appearance cluster A_U^D. We define six appearance clusters: A_F^D (percentage of *sebum dot* pixels $\geq 50\%$ and *red color* ≥ 0.76 in FLUO); A_F^B (percentage of *blotchy* pixels $\geq 50\%$ in FLUO); A_F^S

(percentage of *smooth* pixels $\geq 50\%$ in FLUO); A_U^D (percentage of *sebum dot* pixels $\geq 50\%$ in UV); A_U^B (percentage of *blotchy* pixels $\geq 50\%$ in UV); A_U^S (percentage of *smooth* pixels $\geq 50\%$ in UV).

3.3. Eigenbiome-Model for Skin Microbiome

Using 16S ribosomal RNA gene sequencing [16, 11, 17], a swab from the forehead of each subject is profiled to obtain the relative abundance of 724 genera. Relative abundance of genus is the concentration (percentage) of each of the 289 genus in a subject's skin microbiome. Out of 724 genera, 289 genra had non-zero relative abundance of genus for all the subjects. Subjects with similar microbiome should group together using clustering techniques. However, clustering in a 289 dimensional space is problematic due to the well-known problem in machine learning referred to as the curse of dimensionality. By projecting this high dimensional data to a lower dimensional subspace, we can obtain meaningful clusters that can be linked to appearance. Additionally, the projection provides a convenient visualization.

Principal component analysis (PCA) is widely used for dimensionality reduction. PCA finds an optimal orthogonal basis set for describing the data such that the variance in the
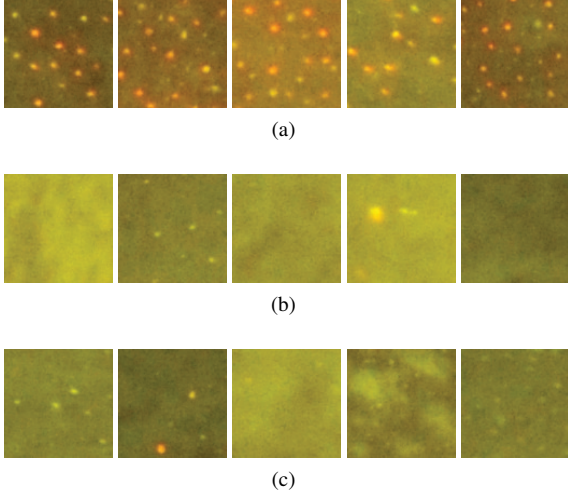
Figure 7: Random samples from the subjects in the three microbiome clusters: (a) Cluster $M1$. (b) Cluster $M2$. (c) Cluster $M3$. Notice that the appearance forms a group in microbiome cluster $M1$. Also see Figure 8.

data is maximized. The data can be projected to a lower dimension with eigenvectors which retain the maximum variance. We refer to the microbiome projected to a lower dimensional eigenspace as *eigenbiome*. For the microbiome data, the percentage of variance retained with each eigenvector is analyzed and it is observed that 92.49% variance is retained by first three eigenvectors. *Thus, three dimensional space is sufficient for this microbiome representation.* Clustering of the eigenbiome is done based on proximity to neighbors by a simple kmeans clustering. The distribution of subjects microbiome in the eigenbiome space suggests clustering with k = 3, i.e., three distinct groups can be visually discriminated. Using three groups, we classify all subjects into one of the three microbiome clusters ($M1$, $M2$ or $M3$) in Figure 8.

The eigenbiome vectors for each of the three clusters have both positive and negative components using PCA. However, the negative concentrations of relative abundance of genus are not physically realizable. If we employ non-negative matrix factorization (NMF) [28], the eigenbiome clusters are constrained to have positive components. This constraint has a very useful physical interpretation. The vector components are positive so that they are *physically realizable* for the relative concentration of genus. Moreover, since NMF favors a sparse solution, the physical interpretation can be enhanced. Sparsity constraints force near zero concentrations to be set to exactly zero. Therefore, the eigenbiome vectors are realizable concentrations of *select* microbes. In this sense the three eigenbiome vectors are distinct microbial communities that contain some microbes,
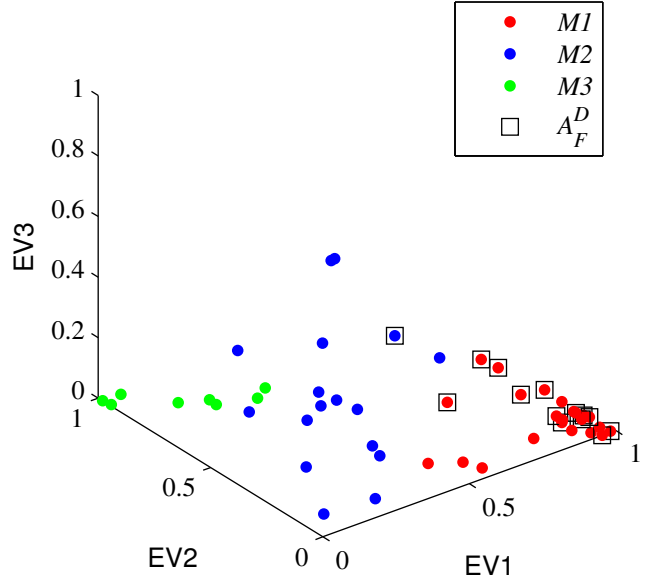

Figure 9: Using non-negative matrix factorization (NMF) for projecting the microbiome to a lower dimensional space, the eigenbiome clusters are constrained to have positive components so that they are physically realizable for the relative concentration of genus. Overlap of microbiome cluster $M1$ and appearance cluster A_F^D (high concentration of sebum dots with red color threshold$\geq$0.76 in FLUO modality) shows that this appearance cluster is linked to microbiome cluster $M1$.

but not others. All subjects are computationally expressed as a mixture of these three dominant communities.

4. Results

Using the computational appearance modeling discussed in Section 3.2, the forehead of a subject in each modality is labeled using the trained NNET classifier and its histogram is obtained as illustrated in Figure 6. The appearance clusters defined by specifying thresholds of attributes. The six appearance clusters, three each for FLUO and UV modalities, are listed in Table 1. These appearance clusters are of interest because our results indicate a clear microbome association. There were not many subjects in the dominant fine-hair category, so a connection to the microbiome could not be made and the category is omitted from Table 1.

Using the eigenbiome model in Section 3.3 each subject is projected to a three dimensional space using PCA and assigned to one of the three microbiome clusters ($M1$, $M2$ or $M3$). Figures 8 shows the overlap of microbiome cluster $M1$ and appearance cluster A_F^D (high concentration of sebum dots with a red color in FLUO modality) shows that
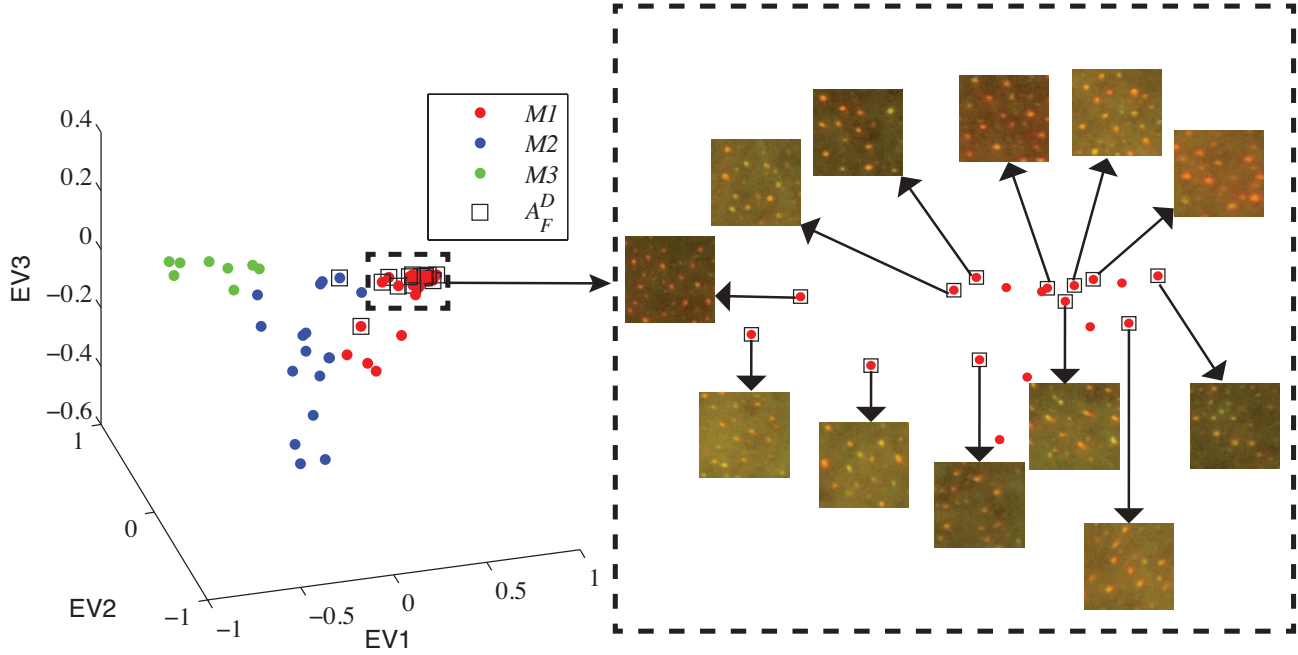
Figure 8: Clusters in eigenbiome have been linked to appearance clusters. (Left) Microbiome is projected to a three dimensional space using PCA and three clusters ($M1(red), M2(blue), M3(green)$) are found using kmeans clustering. The rectangular markings show the appearance cluster A_F^D (high concentration of sebum dots with red color threshold$\geq$0.76 in FLUO modality). Overlap of microbiome cluster $M1$ and appearance cluster A_F^D shows that this appearance cluster is linked to microbiome cluster $M1$. (Right) Example patches are shown for the subjects that are in the overlap of appearance cluster A_F^D and microbiome cluster $M1$. The conditional probabilities such as P($M1 \mid A_F^D$) are given in Table 1. As expected P($M1 \mid A_F^D$) is high showing that appearance is predictable of the microbiome cluster.

Appearance Cluster A		n(A)	P($M1 \mid A$)	P($M2 \mid A$)	P($M3 \mid A$)	P($A \mid M1$)	P($A \mid M2$)	P($A \mid M3$)
A_F^D:	FLUO modality Sebum dot $\geq$ 50% Color $\geq$ 0.76	14	**0.93**	0.07	0	0.57	0.06	0
A_F^B:	FLUO modality Blotchy $\geq$ 50%	5	0	0.6	0.4	0	0.18	0.25
A_F^S:	FLUO modality Smooth $\geq$ 50%	7	0	**0.85**	0.14	0	0.35	0.13
A_U^D:	ULVI modality Sebum dot $\geq$ 50%	29	0.66	0.17	0.17	0.83	0.29	0.63
A_U^B:	ULVI modality Blotchy $\geq$ 50%	12	0.25	0.58	0.17	0.13	0.41	0.25
A_U^S:	ULVI modality Smooth $\geq$ 50%	6	0	**0.83**	0.17	0	0.29	0.13

Table 1: Conditional probabilities for microbiome clusters $M1, M2, M3$ and appearance clusters based on the following appearance attributes: *Dots* - high concentration of sebum dots pixels with red color above threshold, *Blotchy* - high concentration of blotchy pixels and *Smooth* - high concentration of smooth pixels. Observe that the probability of microbiome $M1$ conditioned on appearance cluster A_F^D in FLUO modality with a high concentration of sebum dots and redness=0.76 is 0.93, indicating a 93% chance of a subject being in microbiome cluster $M1$ given this appearance cluster. Similarly observe that the probability of microbiome $M2$ given a high concentration of smooth pixels in FLUO and UV is high (0.85 and 0.83 given A_F^S and A_U^S, respectively.)

this appearance cluster is linked to microbiome cluster $M1$. Using non-negative matrix factorization (NMF) for projecting the microbiome to a lower dimensional space (Figure 9), the eigenbiome clusters are constrained to have positive components so that they are physically realizable for the relative concentration of genus. The subjects grouped together using the projected microbiome data by NMF are same as the subjects in groups using PCA.

Table 1 shows the conditional probability of each of three microbiome clusters conditioned on the individual appearance cluster. High conditional probabilities indicate a high likelihood of the microbiome cluster when the subject exhibits the particular appearance attribute. Observe that in three distinct cases the conditional probability is high: 1) A_F^D: *sebum dots with a red color above the indicated threshold in FLUO* (predictive of microbiome cluster $M1$ with $P(M1 \mid A_F^D)$=0.93); 2) A_F^S: *smooth in FLUO* (predictive of microbiome cluster $M2$ with $P(M2 \mid A_F^S)$=0.85); and 3) A_U^S: *smooth in UV* (predictive of microbiome cluster $M2$ with $P(M2 \mid A_F^S)$=0.83). For the appearance cluster A_F^D) the conditional probability increases as redness of dots increases but the number of samples in the appearance cluster decreases (see Figure 10). Our results reveal a strong link between appearance clusters (captured instantaneously with camera) and microbiome clusters (from time-consuming sequencing).

5. Conclusions

In this paper, we present an attribute-based appearance model using texton-analysis of blue fluorescence and ultraviolet imaging modalities. Using 48 subjects, we link appearance to the eigenbiome, the low dimensional representation of a subject's skin microbiome. The eigenbiome model using non-negative matrix factorization represents physically realizable concentrations of microbes. The intersection of the appearance and eigenbiome clusters reveals three interesting cases where the probability of a subject belonging to a microbiome cluster conditioned on appearance is high. The sequencing of microbiome takes several days but computational appearance is obtained in seconds. The established link to microbiome clusters provides biological information with photographic imaging.
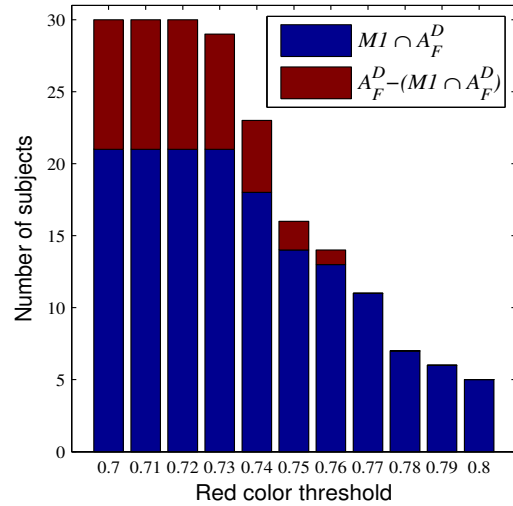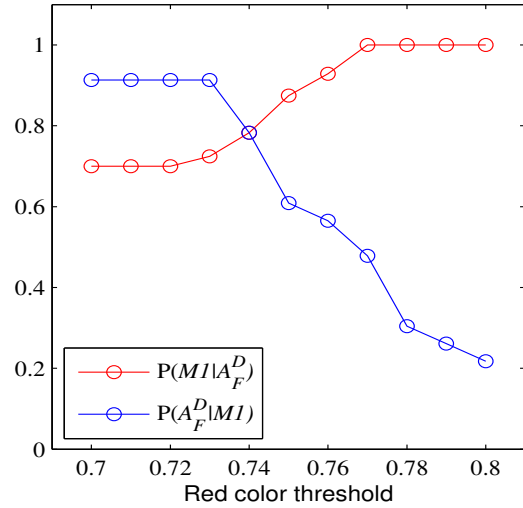
Acknowledgments

(a)

(b)

Figure 10: (a) Conditional probability for linking of microbiome from appearance $P(M1 \mid A_F^D)$ and appearance from microbiome $P(A_F^D \mid M1)$ as a function of redness of dots. For varying threshold of sebum dot redness, appearance cluster A_F^D has subjects with high concentration of sebum dots ($\geq 50\%$) with indicated red color threshold in FLUO. (b) Number of subjects in clusters A_F^D and $M1$ ($M1 \cap A_F^D$) as a function of redness of dots. As the threshold increases, the conditional probability of a subject to be in microbiome cluster $M1$ given it is in appearance cluster A_F^D increases whereas the number of subjects in appearance cluster A_F^D decreases.

References

[1] Z. Akata, F. Perronnin, Z. Harchaoui, and C. Schmid. Label-embedding for attribute-based classification. In *Computer Vision and Pattern Recognition (CVPR), 2013 IEEE Conference on*, pages 819–826, June 2013. 3

[2] Y. Chen and H. Tsao. The skin microbiome: Current perspectives and future challenges. *Journal of the American Academy of Dermitology*, 69(1):143 – 155, 2013. 2

[3] G. O. Cula, P. R. Bargo, and N. Kollias. Imaging inflammatory acne: lesion detection and tracking. *Proc. SPIE*, 7548:75480I–75480I–7, 2010. 3

[4] G. O. Cula, P. R. Bargo, A. Nkengne, and N. Kollias. Assessing facial wrinkles: automatic detection and quantification. *Skin Research & Technology*, 19(1):e243 – e251, 2013. 2

[5] O. G. Cula and K. J. Dana. Compact representation of bidirectional texture functions. *Proceedings of the IEEE Conference on Computer Vision and Pattern Recognition*, 1:1041–1067, December 2001. 3

[6] O. G. Cula and K. J. Dana. 3D texture recognition using bidirectional feature histograms. *International Journal of Computer Vision*, 59(1):33–60, August 2004. 3

[7] O. G. Cula and K. J. Dana. Texture for appearance models in computer vision and graphics. In M. Mirmehdi, X. Xie, and J. Suri, editors, *Handbook of Texture Analysis*. Imperial College Press, 2008. 3

[8] O. G. Cula, K. J. Dana, F. P. Murphy, and B. K. Rao. Skin texture modeling. *International Journal of Computer Vision*, 62(1/2):97–119, April/May 2005. 3

[9] O. G. Cula, K. J. Dana, D. K. Pai, and D. Wang. Polarization multiplexing and demultiplexing for appearance-based modeling. *IEEE Transactions on Pattern Analysis and Machine Intelligence*, 29(2):362–367, February 2007. 3

[10] K. J. Dana, O. G. Cula, and J. Wang. Surface detail in computer models. *Image and Vision Computing*, 25(7):1037 – 1049, 2007. 3

[11] L. Dethlefsen, S. Huse, M. L. Sogin, and D. A. Relman. The pervasive effects of an antibiotic on the human gut microbiota, as revealed by deep 16s rrna sequencing. *PLoS biology*, 6(11):e280, 2008. 5

[12] C. Donner, T. Weyrich, E. d'Eon, R. Ramamoorthi, and S. Rusinkiewicz. A layered, heterogeneous reflectance model for acquiring and rendering human skin. *ACM Trans. Graph.*, 27(5):140:1–140:12, Dec. 2008. 3

[13] L. Fei-Fei and P. Perona. A bayesian hierarchical model for learning natural scene categories. In *Computer Vision and Pattern Recognition, 2005. CVPR 2005. IEEE Computer Society Conference on*, volume 2, pages 524–531 vol. 2, June 2005. 3

[14] S. Fitz-Gibbon, S. Tomida, B.-H. Chiu, L. Nguyen, C. Du, M. Liu, D. Elashoff, M. C. Erfe, A. Loncaric, J. Kim, R. L. Modlin, J. F. Miller, E. Sodergren, N. Craft, G. M. Weinstock, and H. Li. Propionibacterium acnes strain populations in the human skin microbiome associated with acne. *Journal of Investigative Dermatology*, 133(9):2152 – 2160, 2013. 1, 2

[15] A. Ghosh, T. Hawkins, P. Peers, S. Frederiksen, and P. Debevec. Practical modeling and acquisition of layered facial reflectance. *ACM Trans. Graph.*, 27(5):139:1–139:10, Dec. 2008. 3

[16] M. Goodfellow and E. Stackebrandt. *Nucleic acid techniques in bacterial systematics*. J. Wiley, 1991. 5

[17] E. A. Grice, H. H. Kong, G. Renaud, A. C. Young, G. G. Bouffard, R. W. Blakesley, T. G. Wolfsberg, M. L. Turner, and J. A. Segre. A diversity profile of the human skin microbiota. *Genome research*, 18(7):1043–1050, 2008. 5

[18] E. A. Grice and J. A. Segre. The skin microbiome. *Nature Reviews Microbiology*, 9(4):244 – 253, 2011. 2

[19] T. N. H. W. Group, J. Peterson, S. Garges, M. Giovanni, P. McInnes, L. Wang, J. A. Schloss, V. Bonazzi, J. E. McEwen, K. A. Wetterstrand, C. Deal, C. C. Baker, V. Di Francesco, T. K. Howcroft, R. W. Karp, R. D. Lunsford, C. R. Wellington, T. Belachew, M. Wright, C. Giblin, H. David, M. Mills, R. Salomon, C. Mullins, B. Akolkar, L. Begg, C. Davis, L. Grandison, M. Humble, J. Khalsa, A. R. Little, H. Peavy, C. Pontzer, M. Portnoy, M. H. Sayre, P. Starke-Reed, S. Zakhari, J. Read, B. Watson, and M. Guyer. The NIH Human Microbiome Project. *Genome Research*, 19(12):2317–2323, Dec. 2009. 1, 2

[20] B. Han, B. Jung, J. S. Nelson, and E.-H. Choi. Analysis of facial sebum distribution using a digital fluorescent imaging system. *Journal of Biomedical Optics*, 12(1):014006–014006–6, 2007. 3

[21] B. Jung, B. Choi, A. J. Durkin, K. M. Kelly, and J. S. Nelson. Characterization of port wine stain skin erythema and melanin content using cross-polarized diffuse reflectance imaging. *Lasers in Surgery and Medicine*, 34(2):174–181, 2004. 3

[22] H. Kato and T. Harada. Image reconstruction from bag-of-visual-words. In *Computer Vision and Pattern Recognition (CVPR), 2014 IEEE Conference on*, pages 955–962, June 2014. 3

[23] N. Kollias. *Bioengineering of the Skin: Skin Imaging and Analysis*. CRC Press, second edition, 2004. 3

[24] H. H. Kong and J. A. Segre. Skin microbiome: Looking back to move forward. *Journal of Investigative Dermatology*, 132(3 part 2):933 – 939, 2012. 1, 2

[25] K. Korotkov and R. Garcia. Computerized analysis of pigmented skin lesions: A review. *Artificial Intelligence in Medicine*, 56(2):69 – 90, 2012. 2

[26] A. Krishnaswamy and G. V. Baranoski. A biophysically-based spectral model of light interaction with human skin. In *Computer Graphics Forum*, volume 23, pages 331–340. Wiley Online Library, 2004. 3

[27] M. Lai, I. Oru, and J. Barton. The role of skin texture and facial shape in representations of age and identity. *Cortex: A Journal Devoted to the Study of the Nervous System & Behavior*, 49(1):252 – 265, 2013. 2

[28] D. D. Lee and H. S. Seung. Algorithms for non-negative matrix factorization. In *In NIPS*, pages 556–562. MIT Press, 2000. 6

[29] T. Leung and J. Malik. Representing and recognizing the visual appearance of materials using three-dimensional textons. *International Journal of Computer Vision*, 43(1):29–44, 2001. 3, 4

[30] D. Lin and X. Tang. Recognize high resolution faces: From macrocosm to microcosm. In *Computer Vision and Pattern Recognition, 2006 IEEE Computer Society Conference on*, volume 2, pages 1355–1362, 2006. 3

[31] G.-H. Liu, L. Zhang, Y.-K. Hou, Z.-Y. Li, and J.-Y. Yang. Image retrieval based on multi-texton histogram. *Pattern Recognition*, 43(7):2380 – 2389, 2010. 3

[32] S. Madan, K. Dana, and O. Cula. Learning-based detection of acne-like regions using time-lapse features. In *Signal Processing in Medicine and Biology Symposium (SPMB), 2011 IEEE*, pages 1–6, Dec. 2011. 2

[33] S. Madan, K. J. Dana, and G. O. Cula. Multimodal and time-lapse skin registration. *Skin Research And Technology: Official Journal Of International Society For Bioengineering And The Skin (ISBS) [And] International Society For Digital Imaging Of Skin (ISDIS) [And] International Society For Skin Imaging (ISSI)*, 2014. 3

[34] I. Maglogiannis and C. Doukas. Overview of advanced computer vision systems for skin lesions characterization. *Information Technology in Biomedicine, IEEE Transactions on*, 13(5):721–733, Sept 2009. 2

[35] S. Maji, L. Bourdev, and J. Malik. Action recognition from a distributed representation of pose and appearance. In *Computer Vision and Pattern Recognition (CVPR), 2011 IEEE Conference on*, pages 3177–3184, June 2011. 3

[36] S. R. Marschner, S. H. Westin, E. P. Lafortune, K. E. Torrance, and D. P. Greenberg. Image-based brdf measurement including human skin. In *Rendering Techniques 99*, pages 131–144. Springer, 1999. 3

[37] MATLAB Neural Network Toolbox. *version 8.3.0 (R2014a)*. The MathWorks Inc., Natick, Massachusetts, 2014. 4

[38] K. Miyamoto, H. Nagasawa, Y. Inoue, K. Nakaoka, A. Hirano, and A. Kawada. Development of new in vivo imaging methodology and system for the rapid and quantitative evaluation of the visual appearance of facial skin firmness. *Skin Research & Technology*, 19(1):e525 – e531, 2013. 2

[39] J. Niebles, C.-W. Chen, and L. Fei-Fei. Modeling temporal structure of decomposable motion segments for activity classification. In K. Daniilidis, P. Maragos, and N. Paragios, editors, *Computer Vision ECCV 2010*, volume 6312 of *Lecture Notes in Computer Science*, pages 392–405. Springer Berlin Heidelberg, 2010. 3

[40] S. Nina N. and G. Richard L. Review: Structure and function of the human skin microbiome. *Trends in Microbiology*, 21:660 – 668, 2013. 2

[41] G. Patterson and J. Hays. Sun attribute database: Discovering, annotating, and recognizing scene attributes. In *Computer Vision and Pattern Recognition (CVPR), 2012 IEEE Conference on*, pages 2751–2758, June 2012. 3

[42] L. Pishchulin, A. Jain, M. Andriluka, T. Thormahlen, and B. Schiele. Articulated people detection and pose estimation: Reshaping the future. In *Computer Vision and Pattern Recognition (CVPR), 2012 IEEE Conference on*, pages 3178–3185, June 2012. 3

[43] A. Sadovnik, A. Gallagher, D. Parikh, and T. Chen. Spoken attributes: Mixing binary and relative attributes to say the right thing. In *Computer Vision (ICCV), 2013 IEEE International Conference on*, pages 2160–2167, Dec 2013. 3

[44] M. Silveira, J. Nascimento, J. Marques, A. R. S. Marcal, T. Mendonca, S. Yamauchi, J. Maeda, and J. Rozeira. Comparison of segmentation methods for melanoma diagnosis in dermoscopy images. *Selected Topics in Signal Processing, IEEE Journal of*, 3(1):35–45, Feb 2009. 2

[45] M. Varma and A. Zisserman. Texture classification: are filter banks necessary? In *Computer Vision and Pattern Recognition, 2003. Proceedings. 2003 IEEE Computer Society Conference on*, volume 2, pages II–691–8 vol.2, 2003. 3

[46] H. Wang, A. Klser, C. Schmid, and C.-L. Liu. Dense trajectories and motion boundary descriptors for action recognition. *International Journal of Computer Vision*, 103(1):60–79, 2013. 3

[47] T. Weyrich, W. Matusik, H. Pfister, B. Bickel, C. Donner, C. Tu, J. Mcandless, J. Lee, A. Ngan, H. Wann, and J. M. Gross. Analysis of human faces using a measurement-based skin reflectance model. *ACM Transactions on Graphics*, 25:1013–1024, 2006. 3

[48] J. Wu and J. Rehg. Beyond the euclidean distance: Creating effective visual codebooks using the histogram intersection kernel. In *Computer Vision, 2009 IEEE 12th International Conference on*, pages 630–637, 2009. 3

[49] X. Wu, D. Xu, L. Duan, and J. Luo. Action recognition using context and appearance distribution features. In *Computer Vision and Pattern Recognition (CVPR), 2011 IEEE Conference on*, pages 489–496, June 2011. 3

[50] Y. Yang and D. Ramanan. Articulated pose estimation with flexible mixtures-of-parts. In *Computer Vision and Pattern Recognition (CVPR), 2011 IEEE Conference on*, pages 1385–1392, June 2011. 3

[51] Y. Zhang, Z. Jia, and T. Chen. Image retrieval with geometry-preserving visual phrases. In *Computer Vision and Pattern Recognition (CVPR), 2011 IEEE Conference on*, pages 809–816, June 2011. 3